



Electrospinning of silica sub-microtubes mats with platinum nanoparticles for NO catalytic reduction

Ramiro Ruiz-Rosas^a, Juana M. Rosas^a, Ignacio G. Loscertales^b, José Rodríguez-Mirasol^{a,*}, Tomás Cordero^a

^a University of Málaga, Andalucía Tech, Chemical Engineering Department, Campus de Teatinos, 29071 Málaga, Spain

^b University of Málaga, Andalucía Tech, Department of Mechanical Engineering and Fluids Mechanic, Campus de Teatinos, 29071 Málaga, Spain



ARTICLE INFO

Article history:

Received 8 November 2013

Received in revised form 21 February 2014

Accepted 26 February 2014

Available online 7 March 2014

Keywords:

Coaxial electrospinning

Silica nanotubes

Platinum nanoparticles

NO_x SCR

ABSTRACT

Silica sub-microtubes loaded with platinum nanoparticles have been prepared in flexible non-woven mats using co-axial electrospinning technique. A partially gelated sol made from tetraethyl orthosilicate was used as the silica precursor, and oil was used as the sacrificial template for the hollow channel generation. Platinum has been supported on the wall of the tubes just adding the metallic precursor to the sol-gel, thus obtaining the supported catalyst by one-pot method. The silica tubes have a high aspect ratio with external/internal diameters of 400/200 nm and well-dispersed platinum nanoparticles of around 2 nm. This catalyst showed a high NO conversion with very high selectivity to N₂ at mild conditions in the presence of excess oxygen when using C₃H₆ as reducing agent. This relevant result reveals the potential of this technique to produce nanostructured catalysts onto easy to handle conformations.

© 2014 Elsevier B.V. All rights reserved.

1. Introduction

One dimensional nano- and sub-microstructured materials, such as fibers, wires or tubes show novel and interesting physical and chemical properties, which make them promising materials for applications in semiconductor, energy storage, sensor, optics or catalysis and play an important role in fundamental research [1–4]. In catalytic processes, pore diffusion resistance is significant in pellet shaped catalysts, while powdered catalysts, as is the practice in most laboratory-scale studies, are very hard to handle and could cause problems of high pressure drop in industrial size reactors. Therefore, novel forms of catalyst supports, as sub-microtubes catalysts, which are easy to handle, can be packed or constructed in the best form to fit the particular use and show very low resistance to diffusion [5], represent a key research issue for many catalytic industrial processes.

In this sense, electrospinning is a simple technique that has been used to obtain polymer and carbon fibers and tubes in the submicro- and nanoscale [6–11], in which a solution held in a capillary tube by its surface tension is subjected to an electric field that stretches the electrified jet due to the electrostatic repulsions

between the surface charges and the evaporation of the solvent. The action of the electric field over a drop, forming at the tip of a capillary, changes its shape into a charged conical meniscus known as the Taylor cone [9]. Parameters such as viscosity and concentration of electrospun solution, flow rate and applied voltage control the diameter and length of fibers/tubes.

Moreover, using a co-axial electrospinning setup makes possible to switch from steady electrospray (droplets) to electrospinning (fibers/tubes) just controlling flow rate between outer and inner solutions. It also allows encapsulating of core liquid and the production of tubes [12,13]. The sol-gel technique has been widely studied for the preparation of different forms including monoliths, powders, coatings, and fibers [14,15]. In the case of silica forms, the typical sol-gel method consists of the hydrolysis and condensation of tetraethyl orthosilicate (TEOS), Si(OCH₂CH₃)₄.

In order to turn spinnable a solution is rather common to add some additives in the formulation, i.e., salts to improve conductivity or polymers to modulate the viscosity. This approach can also be profited to easily deposit metal catalysts on fiber/tubes just adding the metal precursor to the solution [11]. The presence of metal nanoparticles on the electrospun fiber/tube displays a huge potential in the area of heterogeneous catalysis. The diffusional constraints that can be found on most widely used catalyst conformation, i.e., spheres, pellets or layers over the wall of monoliths, may be reduced if the active phase is supported over

* Corresponding author. Tel.: +34 951 952 385; fax: +34 951 952 385.

E-mail address: mirasol@uma.es (J. Rodríguez-Mirasol).

the external walls of electrospun submicrosized fibers. Moreover, fibers could be directly casted as thin films over a support, or in form of flexible non-woven fabrics, which can be easily handled and deployed in any catalytic system.

Selective catalytic reduction (SCR) of NO to N₂ is a well-established technique readily available for the control of NO_x emissions in stationary sources. SCR of NO_x with hydrocarbons (HC-SCR) at low temperature ($T < 300^{\circ}\text{C}$) under strongly oxidizing conditions is still a challenge and extensively studies have been carried out in the last years [16–18]. This technology seems to be especially suited for the case of emission control in diesel where more complete fuel combustion at excess oxygen and lower temperatures takes place, improving fuel economy. Platinum seems to be the most active metal for this case [19]. However, the main drawbacks of these Pt-based catalytic systems are the high selectivity to N₂O at low reaction temperatures and a narrow window of temperatures where high enough NO_x conversion is achieved. The platinum particle size, oxidation state and the interaction with the support play an important role in the NO_x reduction mechanism through the hydrocarbon activation over the catalyst surface [19–21]. More specifically, platinum supported on silica catalysts are reported to have a medium to high activity for NO_x propylene-SCR, also showing higher chemical stability than alumina-supported catalysts when water or sulfur dioxide is present in the gas stream [22,23]. Nevertheless, activity and N₂ selectivity on NO_x HC-SCR at low temperature for Pt-SiO₂ catalytic system are still to be enhanced.

In this work, we present the preparation and characterization of silica sub-microtubes with and without platinum nanoparticles using a sol-gel method followed by a coaxial-electrospinning process. One-dimensional structured materials with well dispersed platinum nanoparticles were obtained by a simple and straightforward one-pot process. Silica sub-microtubes with 1% platinum were used as catalysts for NO reduction with propylene in the presence of oxygen.

2. Materials and methods

2.1. Catalyst preparation

The silica sol was prepared from TEOS, ethanol, distilled water, and HCl. The sol composition in molar ratio was 1:2:2:0.025 (TEOS:ethanol:water:HCl). First, the HCl was mixed with water. Once diluted, ethanol was added to the solution. This solution is added to the TEOS. The acid catalyzes the hydrolysis reaction, which is strongly exothermic, and the TEOS is dissolved. The mixture, stirred vigorously, was heated up to 80 °C for 1 h and then cooled down to 60 °C. In the case of the tubes containing platinum, platinum (II) acetylacetone was added to the solution at 60 °C in a molar ratio to TEOS of 0.006. The solutions (with and without platinum) were maintained at this temperature under stirring for approximately 48 h in order to evaporate the alcohols formed during the condensation phase of the sol gel and to reach the viscosity required for turning the gel spinnable by this technique. By this way, the solidification of the partially gelated TEOS during the fly of the jet to the collector is ensured, thus avoiding the breaking up of the jet because the prevalence of a varicose instability. Silica sub-microtubes were generated by using the coaxial electrospinning method reported in the literature [12] in a co-axial configuration, with the sol gel, which plays the role of carrier, coming through the external capillary tip and synthetic oil flowing through the inner one (Fig. 1). Both liquid viscosities were high enough to allow the viscous forces to overcome the liquid–liquid surface tension so the TEOS gel can drag the oil template, forming a compound Taylor cone [12]. The synthetic oil will act as a template fluid producing

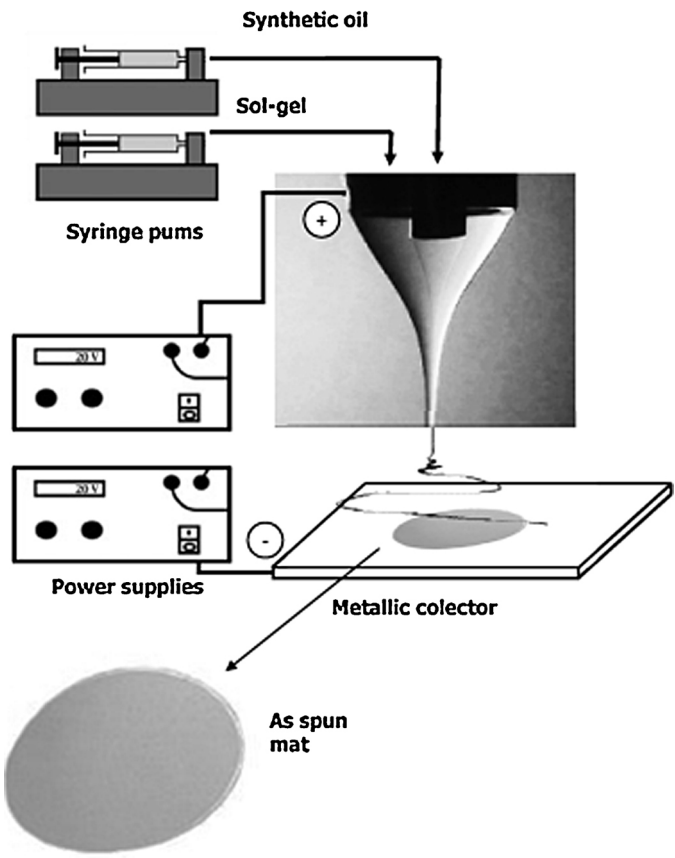


Fig. 1. Coaxial electrospinning set up for the preparation of the catalysts.

the tube conformation after its removal. The flow rates through the needles were around 0.6/1.5 mL h⁻¹ for sol gel/synthetic oil, respectively. To apply the high voltage between the spinneret and the collector (Fig. 1), two high voltage power supplies are used: one positively polarized connected to the needle and the other negatively polarized attached to a collector. This configuration provided better electrostatic conditions to prevent tubes from flying to any grounded piece near the set-up, therefore facilitating the deposition of the electrospun tubes on the collector. The tip-to-collector distance was 20–25 cm, and the electrical potential difference was 10 kV (the collector was at -5 kV and the tips at +5 kV), although this value could slightly varied depending on the collector/tip geometry.

The electrospun tubes with and without platinum were easily collected as a flexible non-woven mat, Fig. 1, and are referred as SiT-Pt and SiT, respectively. Finally, the electrospun tubes were calcined at 500 °C for 2 h in a muffle furnace, in order to eliminate the solvents and the synthetic oil and stabilize the silica tubes. Silica nanotubes with and without platinum are denoted as SSiT-Pt and SSiT, respectively. The stabilized (calcined) electrospun mats acquired a cotton-like texture, and although they turned more brittle under mechanical pressure, they kept enough mechanical stiffness and flexibility to allow their easy manipulation without compromising the structural integrity of the mat.

2.2. Catalyst characterization

Thermogravimetric analysis (TG) was performed in a CI Electronics MK2 balance under air flow (150 cm³ STP/min) from room temperature to 900 °C at a heating rate of 10 °C/min with a sample weight of about 10 mg. X-ray diffraction patterns (XRD) were

recorded in the region of $2\theta = 5\text{--}80^\circ$ on a Philips X'Pert PRO MPD diffractometer using CuK α monochromatic radiation (operation value 45 kV and 40 mA).

The porous structure was characterized by N₂ adsorption-desorption at -196°C and by CO₂ adsorption at 0°C , carried out in a Micromeritics ASAP2020 apparatus. Samples were previously outgassed for 8 h at 150°C under vacuum. From the N₂ adsorption/desorption isotherm, the apparent surface area (A_{BET}) was calculated by applying the BET equation. Micropore volume (V_{DR}) was estimated by applying the Dubinin–Raduskevich equation on the low pressure adsorption branch [24], while the application of t method using Harkins and Jura equation allows the estimation of external surface area (A_t). CO₂ adsorption isotherm at 0°C was used to assess the narrow micropore surface area, $A_{\text{DR(CO}_2\text{)}}$, and micropore volume, $V_{\text{DR(CO}_2\text{)}}$. The surface chemistry of the samples was studied by X-ray photoelectron spectroscopy (XPS) analysis, using a 5700 C model Physical Electronics apparatus with MgK α radiation (1253.6 eV). For the analysis of the XPS peaks, the C 1s peak position was set at 284.5 eV and used as reference to locate the other peaks. The fitting of the XPS peaks was done by least squares using Gaussian–Lorentzian peak shapes. Fourier transform infrared (FTIR) spectra were obtained using a Bruker Optics Tensor 27 FT-IR spectrometer by adding 256 scans in the $4000\text{--}400\text{ cm}^{-1}$ spectral range at 4 cm^{-1} resolution. Pressed KBr pellets at a sample/KBr ratio of around 1:250 were used.

The surface and inner morphology of the tubes was studied by scanning electron microscopy (SEM) using a JSM 840 JEOL microscope working at 25 KV voltage and by transmission electron microscopy (TEM) in a Philips CM200 microscope at an accelerating voltage of 200 kV and in a high angle annular dark field (HAADF) FEI Titan G2. The mean diameter of the silica tubes as well as their wall size were determined from TEM images (more than fifty different tubes were examined), while the platinum size distribution of the SSiT-Pt sample was obtained by counting 95 particles. The size distribution was fitted to a normal distribution. From the size distribution, we determined the average diameter [25]. Platinum particle size (assuming spherical particles) and dispersion (D) are related by $D = 108/dn$ (nm) [26].

2.3. NO selective catalytic reduction (SCR) experiments

The NO reduction experiments were performed in a quartz fixed bed microreactor (4 mm i.d.) at atmospheric pressure. Experiments were carried out with 80 mg of stabilized tubes (SSiT or SSiT-Pt). The inlet flow rate used was $200\text{ cm}^3 \text{ STP/min}$, with NO concentration of 400 ppm, resulting in a space time of $W/\text{FNO} = 2.88\text{ g s}/\mu\text{mol}$. The concentrations of other inlet gases were 3% for O₂, 1500 ppm for C₃H₆ and 1000 ppm for SO₂. A chemiluminescent analyzer (Eco-Physics, CLD 700 AL model) was used to measure the outlet gas concentrations of NO and NO₂. The SO₂, CO and CO₂ outlet concentrations were analyzed by means of a non-dispersive infra-red analyser (Ultramat 22, Siemens model). C₃H₆, H₂O, N₂, N₂O and O₂ concentrations were measured by a mass spectrometer analyzer (Balzers MsCube).

3. Results and discussion

3.1. Air calcination of as-spun mats

TGA experiments were conducted over the as-spun tubes for selecting a desirable air calcination temperature. Fig. 2 represents the weight loss of the silica tubes with and without platinum and of the synthetic oil used as template in the electrospinning process as a function of temperature, from room temperature to 900°C , at a heating rate of $10^\circ\text{C}/\text{min}$ in air atmosphere. TGA results revealed

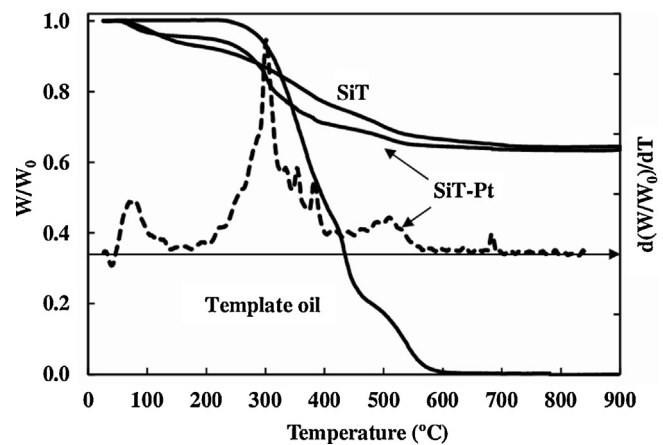


Fig. 2. TG profiles in air atmosphere of the as-spun sub-microtubes with and without platinum and the synthetic oil used as template (left axis). DTG profile of the SiT-Pt sample (right axis).

different steps in the degradation of the template oil under oxygen atmosphere, probably corresponding to decomposition of unsaturated and saturated fatty acids which are the main component of oils [27] and also the oxidation of carbon residue. In the case of the tubes, the mass loss begins at temperatures lower than 100°C due to the evaporation of the solvents used in the formulation of the silica tubes. The TGA profiles for the tubes show a significant mass loss, beginning at around 300°C and finishing at about $500\text{--}600^\circ\text{C}$, matching those observed for the synthetic oil used as template and, therefore, associated to the decomposition and oxidation of the oil remaining in the inner of the non stabilized silica tubes. This mass loss is more pronounced and starts at lower temperature for the SiT-Pt tubes than for the SiT ones, probably as a consequence of the catalytic effect of the platinum in the decomposition and oxidation reaction. The slow weight loss observed for the tubes with increasing temperature up to 700°C is probably due to the water molecules released during the self-condensation reaction of the silanol groups [28]. Derivative thermogravimetric analysis (DTG) obtained from the calcination curve of the SiT-Pt sample revealed the maximum weight loss rate for the last calcination step of the curve lies at 500°C . Therefore, this temperature was set as the final one for air calcination of the silica tubes.

3.2. Nanotubes morphology

The morphology of the prepared mats was analyzed by SEM. Fig. 3a–d show selected micrographs of the SiT, SSiT and SSiT-Pt samples. It can be seen that these mats consist in a non-woven fabric of submicrometric tubes. The size and shape of these tubes were very uniform in the as-spun mat, and no sintering or beads were found (Fig. 3a). Furthermore, the tubes show a high aspect ratio (ratio between the length and the external diameter of the tubes), with diameters clearly lower than 1 μm . Neither the calcination process nor the introduction of platinum show a significant influence on the morphology or size of the resulting fibers, Fig. 3b and c. Fig. 3d provides evidence of the hollow channel induced by the template removal in these forms, which can be seen at the tip of some broken tubes.

Co-axial electrospinning is a powerful technique to prepare tubes of controlled sizes. The wall width can be adjusted by fine-tuning the delivery rate of the template and gel to the Taylor cone. Varying the template/gel flow ratio between 1/1 and 3.5/1 while keeping the carrier rate at 0.6 mL h^{-1} caused an increase in both the size of the channel inside the silica fiber and the external diameter. When oil was fed at rates lower than 0.8 mL h^{-1} , the occurrence of

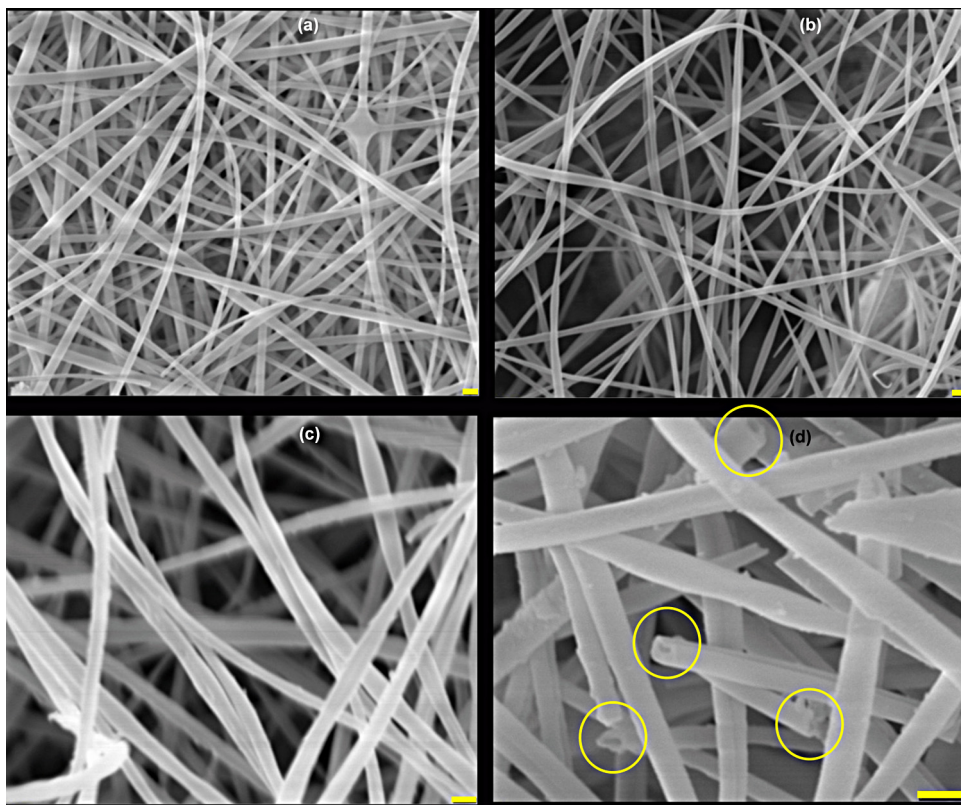


Fig. 3. SEM images of (a) SiT, (b) SSiT, (c) and (d) SSiT-Pt (bars length: 1 μm).

inner dripping mode started to happen (i.e., the outer liquid encapsulates the inner one in small droplets). On the other hand, delivery rates over 1.6 mL h⁻¹ further reduced the silica wall thickness to values lower than 100 nm, but caused the appearance of shape and size irregularities. The delivery rates were set to 0.6 and 1.6 mL h⁻¹ for the TEOS and oil template solutions, respectively, seeking to ensure a continuous tube shape. Fig. 4a displays TEM images of several nanotubes of SiT. They seem to be uniform, lacking structural defects and showing a high aspect ratio. Fig. 4b represents a higher magnification TEM image of a silica tube obtained after air calcination. This tube shows likewise an external diameter of 346 nm and a channel width of 122 nm. The average external diameters of SiT and SSiT were 397 ± 74 and 378 ± 64 nm, respectively, with wall sizes of 108 ± 19 and 103 ± 17 nm, proving that calcination did not substantially modify the morphology of the tubes. The selected-area electron diffraction pattern (SAED) of the stabilized tubes (detail in Fig. 4b) shows no diffraction patterns, pointing out the amorphous structure of the silica tubes.

The huge flexibility and control that electrospinning brings over the decoration of platinum nanoparticles is reflected in the TEM images in Fig. 4c and d. In the formulation of the mat showed in this image, a platinic salt was added in the TEOS gel. Consequently, after the removal of the oil template during the calcination process, silica tube decorated with platinum nanoparticles were obtained. The addition of the platinum salt in the sol-gel precursor did not affect substantially the morphology of the nanotubes, showing average diameters and wall sizes of 386 ± 69 and 116 ± 17 nm for the SSiT-Pt sample. Platinum nanoparticles were preferentially found on the internal wall of the tubes, Fig. 4c. Fig. 4d shows a high-angle annular dark field scanning transmission electron microscopy (HAADF-STEM) image of the wall of the stabilized tube with platinum. A high amount of spherical dark spots that are very well-dispersed can be observed in this figure, with sizes approximately between 1.5 and 3.5 nm.

HAADF-STEM was calibrated by energy-dispersive X-ray spectroscopy (EDX) measurements to also obtain the compositional dispersion of platinum nanoparticles shown in Fig. 5a. The analysis of the area represented in this micrograph revealed the presence of 1.4 wt.% of platinum, uniformly distributed.

Fig. 5b and c collects the HRTEM image and the selected electron diffraction pattern of the Pt nanoparticles. The crystallinity of platinum is well observed in Fig. 5b. The lattice spacing of 0.23 and 0.196 nm agree with the distance between two (1 1 1) and two (2 0 0) planes of platinum metallic, respectively. The corresponding SAED of the silica sub-microtubes loaded with platinum nanoparticles shows a highly diffusive ring pattern due to the low presence and size and, consequently, high dispersion of platinum nanoparticles. However, some single diffraction spots can be observed and associated to the diffraction from the (2 0 0) plane of crystalline Pt particles.

Fig. 5d shows the platinum particle size distribution histogram. It has been fitted to a normal distribution with mean diameter, μ , and standard deviation σ . Based on this measurement, the average diameter size was 2.4 nm and the dispersion of the platinum is as high as 45%.

The benefits of using tubes instead of solid fibers when bringing accessibility to the active phase of a catalyst system can be illustrated in terms of their respective Thiele modulus. The ratio between Thiele modulus, φ , for hollow to solid fibers is described as follows:

$$\frac{\varphi_{\text{hollow}}}{\varphi_{\text{solid}}} = \frac{W_{\text{hollow}}/2}{Rf_{\text{solid}}} \cdot \frac{\sqrt{k \cdot C^{n-1}/D_e}}{\sqrt{k \cdot C^{n-1}/D_e}} = \frac{w_{\text{hollow}}}{Rf_{\text{solid}}}$$

where k , C^{n-1} and D_e stands for the kinetic rate, the bulk concentration of the reactive and the effective diffusivity, respectively. On the other hand, Rf_{solid} is the solid fiber radius, while w_{hollow} is the wall thickness of the tube, which is divided by 2 since the wall is

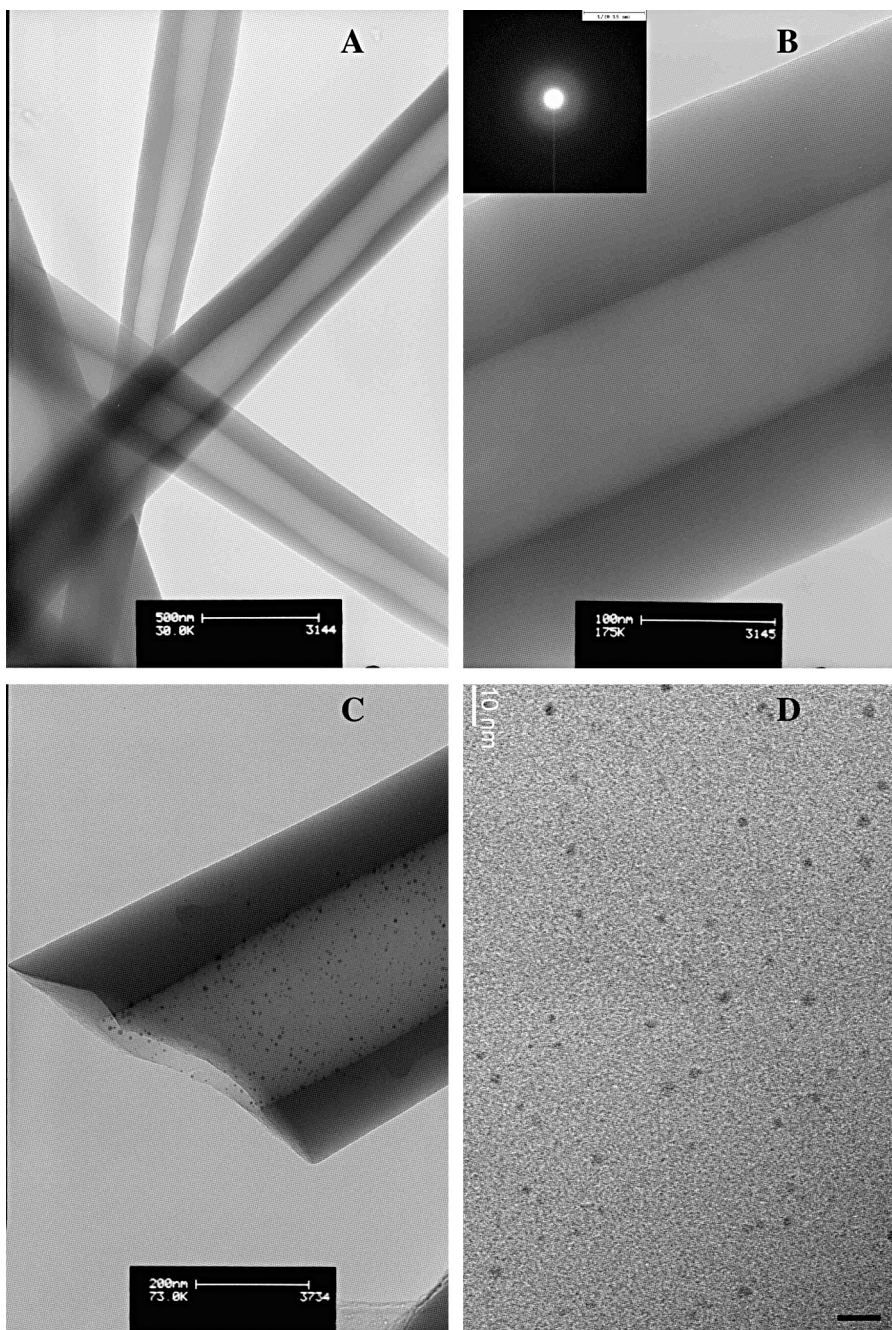


Fig. 4. TEM images of (a) SiT (bar length: 500 nm), (b) SSiT (bar length: 100 nm), (c,d) SSiT-Pt (bars length: 200 and 10 nm, respectively).

accessible from both sides, thus reducing by half the molecular pathway inside it. Since in both fiber and tube porosity, pore size distribution and connectivity are the same and the catalyst is evenly distributed, those parameters are to be equal for both conformations. Therefore the tube to fiber Thiele modulus ratio is $50/200 = 0.25$. The generation of the channel inside the fiber results in an important improvement on availability of the catalyst. As an outcome it can be claimed that the tube with external/internal diameters of 400/200 nm should face the same diffusional constraints than a 100 nm solid one.

3.3. Catalyst characterization

Fig. 6 represents the FTIR spectrum of the non-stabilized and stabilized tubes with and without platinum. Broad transmission

bands between 4000 and 3000 cm^{-1} are observed which correspond to the fundamental stretching vibrations of different types of hydroxyl groups [29]. The spectra clearly show two bands at 795 and 950 cm^{-1} associated to Si—O vibration in silanol groups (Si—OH). The bands at 1082 cm^{-1} are related to Si—O—Si groups. These groups are formed due to the hydrolysis and condensation of TEOS. After the calcination step, a decrease in the Si—OH band and an increase in the Si—O—Si band are obtained due to the complete condensation of hydrolyzed silica precursor (Si—OH) to silica (SiO_2) [30]. The band at 1625 cm^{-1} could be related to the combination of the SiO_2 vibrational modes. It should be noted the low intensity of the bands related to methyl (CH_3) or methylene (CH_2) located at around 2800–3000 and 1400–1800 cm^{-1} , respectively, on the as-spun fibers, related to a low contribution of methyl or methylene of ethoxy groups ($-\text{OCH}_2\text{CH}_3$), suggests that most of the TEOS is

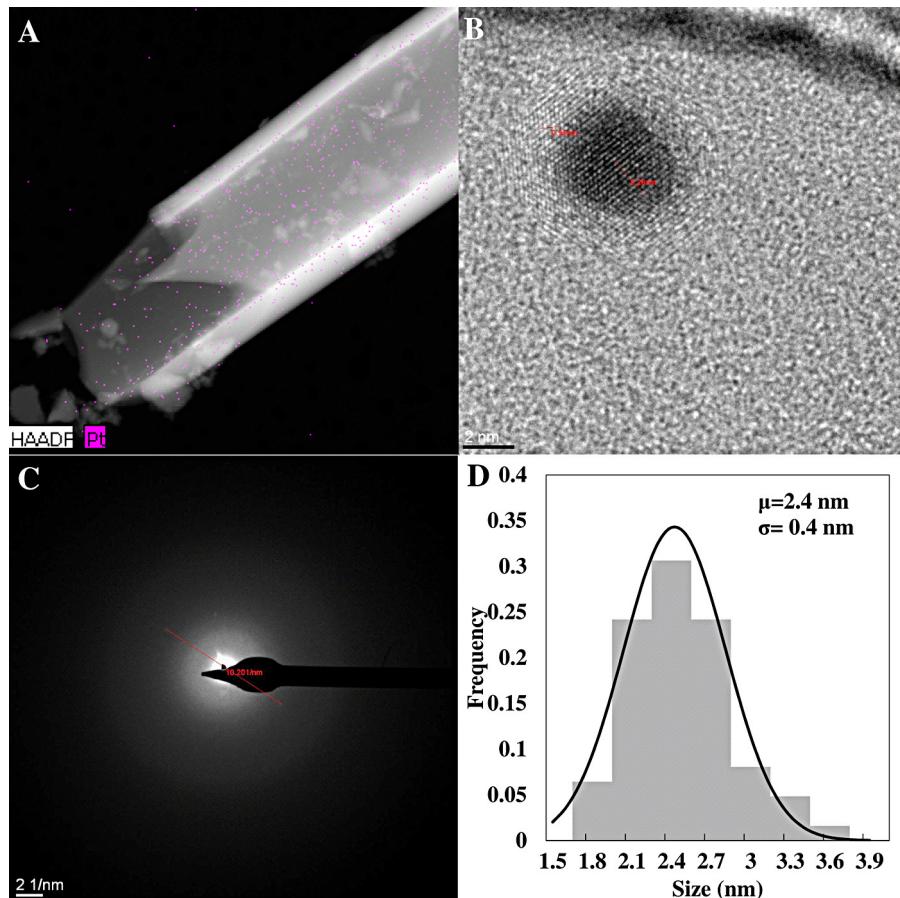


Fig. 5. (a) HAADF-STEM of an SSiT-Pt tube, (b) high resolution TEM image of a platinum nanoparticle (bar length: 2 nm), (c) SAED registered from a platinum loaded silica nanotube, (d) platinum particle size distribution histogram of the SSiT-Pt sample.

hydrolyzed. These bands have not fully disappeared in the spectra of the stabilized fiber, probably due to incomplete decomposition and oxidation of the organic compounds (solvents and template oil) of the tubes during the calcination process.

The porous structure of the different tubes was analyzed by N_2 adsorption-desorption isotherms at -196°C and CO_2 adsorption at 0°C , and the results are shown in Table 1. The electrospun tubes with and without platinum, SiT-Pt and SiT respectively, show very low BET areas, as in non-porous solids. The similar values obtained for external surface area, A_t , and apparent surface area, A_{BET} , is manifesting that nitrogen is adsorbing mainly in the geometrical exposed area of the tube. The comparison of the apparent surface area obtained from the N_2 and CO_2 adsorption isotherms, with $A_{\text{DR}(\text{CO}_2)} \gg A_{\text{BET}}$, points out the presence of microporosity in these

tubes, with mean pore size values under 0.7 nm [31]. The calcination process of SiT seems to produce the shrinkage of this narrow microporous structure. However, the presence of the platinum precursor results in a development of wide microporosity, measured with N_2 adsorption, resulting in silica tubes with total BET surface area of $144 \text{ m}^2/\text{g}$. Lin et al. [32] reported that the addition of low Pt salt concentrations to the electrospinning of polyacrylonitrile/platinum acetylacetone solution could increase the fiber diameters, due to the formation of polymer–salt–solvent interactions, which changed the balance among the viscosity, surface tension, and conductivity of the synthesis solutions. Unfortunately, they did not analyze the influence of the Pt salt on the fibers porosity. However, the porosity increase of the silica tubes can be ascribed to the decomposition of the platinum salt, which could act as a porosity template. In this sense, the work of Katz and Davis is a good example of the possibilities for tailoring microporosity opened by molecular imprinting of silica host by controlled addition of organic ligands during the sol–gel synthesis, which will create cavities in the silica matrix when removed in a subsequent etching step [33].

Fig. 7a shows the C 1s spectra for the as-spun and air-stabilized silica tubes. The presence of platinum does not modify significantly the C 1s spectra. The deconvoluted spectrum of the as-spun fibers show three different peaks, (i) at 284.5 eV associated to C–C and C–H bonds [34], (ii) at around 286.1 eV that could be related to C–OH groups [34] present in the ethanol used in the precursor solution and produced by the hydrolysis reaction of TEOS and (iii) at approximately 288.7 eV associated to the C–Si–O groups [29] from residual TEOS after the tube formulation. The calcination process removes almost all the carbon groups due to the evaporation

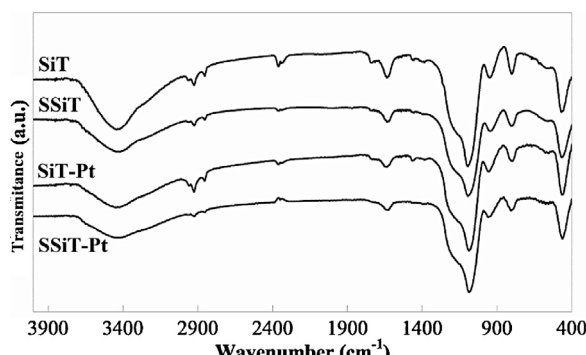


Fig. 6. FTIR spectra of as-spun and calcined samples.

Table 1

Porous structural parameters of different silica sub-microtubes with and without platinum obtained from N₂ and CO₂ isotherms.

Sample	$A_{\text{BET}(\text{N}_2)}$ (m ² /g)	$A_{\text{t}(\text{N}_2)}$ (m ² /g)	$A_{\text{DR}(\text{CO}_2)}$ (m ² /g)	$V_{\text{DR}(\text{N}_2)}$ (cm ³ /g)	$V_{\text{DR}(\text{CO}_2)}$ (cm ³ /g)
SiT	3	2	228	–	0.087
SSiT	7	4	135	0.001	0.051
SiT-Pt	3	2	121	–	0.046
SSiT-Pt	144	13	273	0.056	0.104

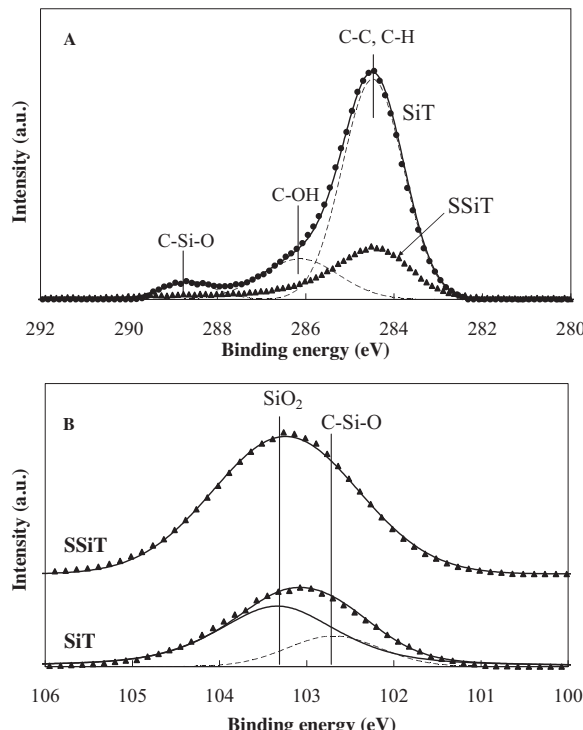


Fig. 7. Deconvoluted XPS C 1s (a) and Si 2p (b) spectra of as spun and calcined silica tubes.

of remaining ethanol and to the oxidation of the ethoxy groups and the organic compounds present in the synthetic oil, used as template of the tube. Thus, the C 1s spectra of the stabilized tubes presents a main peak located at 284.5 eV probably due to adventitious carbon. The deconvoluted Si 2p spectra of SiT and SSiT tubes are also represented in Fig. 7b. The spectrum of the as-spun nanotubes show a shift to lower binding energies that can be related to the presence of carbon atoms bonded to silicon. The chemical shift in the Si 2p photoelectron signal is mainly induced by the number of oxygen atoms bound to a Si atom. When introducing carbon atoms into SiO₂, some of the four oxygen atoms bonded to the silicon are replaced by carbon atoms and the Si 2p spectra shifts to lower binding energy values [35,36]. Furthermore, a slight asymmetry of the spectrum of as-spun tubes is observed. According to Ingo el al. [37], it could be associated to the presence of Si—O—CH₂CH₃ bonds from the precursor solution and it disappears when the sol-gel materials are subjected to air thermal treatments at temperatures higher than 400 °C. This supports the presence of residual TEOS on the as-spun SiT sample. After air stabilization, the organic matter has been removed and all the silicon is in form of SiO₂.

Table 2 summarizes the atomic surface concentrations obtained from the numerical integration of the XPS peaks for the different silica tubes. The amount of surface silicon is much lower than that of carbon and oxygen for the non stabilized tubes. The stabilized (calcined) samples show much lower carbon content than that of the non-stabilized tubes, confirming the removal of organic compounds of the synthetic oil and the decomposition of remaining

Table 2

Atomic surface concentration (%) of different silica sub-microtubes with and without platinum determined by XPS quantitative analysis.

Sample	%C	%O	%Si	%Pt
SiT	48.6	35.5	15.9	–
SSiT	11.0	60.5	28.5	–
SiT-Pt	57.7	31.7	10.6	0.0(4)
SSiT-Pt	9.8	60.1	30.0	0.1(2)

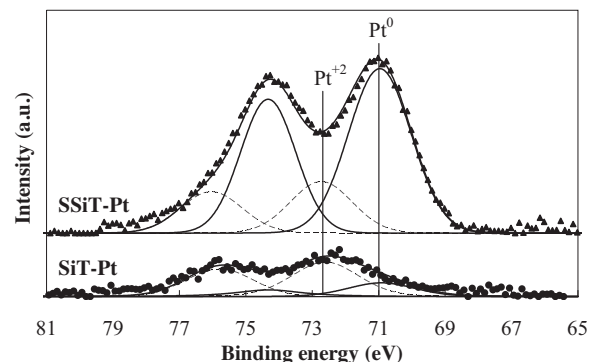


Fig. 8. Deconvoluted XPS Pt 4f spectra of Pt-loaded samples.

ethoxy groups and solvents on the sol-gel. The O/Si atomic ratio obtained after calcination is that corresponding to silica. In the case of the mats that contain platinum, the amount of surface platinum increases with the stabilization process, as a consequence of the removal of the organic part of the nanotubes. The platinum/silicon atomic ratio keeps constant at 0.004, which is lower than the value of 0.006 corresponding to the Pt/Si atomic ratio of the Pt(AcAc)₂/TEOS initial solution. The stabilized silica tubes with platinum show a platinum atomic surface concentration of 0.12%, which corresponds to a weight surface concentration of 1.20%, somehow lower than that of the theoretical value from the tubes formulation, 1.91%. This result and the relatively high surface area value obtained for the $A_{\text{DR}(\text{CO}_2)}$ value from 228 m²/g for SiT to 121 m²/g for SiT-Pt (Table 2) suggests that the Pt precursor is located in part of the micropores. After calcination of SiT-Pt, the value of $A_{\text{DR}(\text{CO}_2)}$ increases to 273 m²/g, as a consequence of Pt precursor decomposition, with a significant increase of the $A_{\text{BET}(\text{N}_2)}$ to 144 m²/g.

The oxidation state of platinum was studied by XPS. Fig. 8 displays the Pt 4f spectra for the Pt containing non-stabilized and stabilized tubes. The Pt 4f region of these tubes presents a doublet corresponding to Pt 4f_{7/2} and Pt 4f_{5/2} [34]. The separation between Pt 4f_{7/2} and Pt 4f_{5/2} peaks, due to spin orbital splitting, is a quantized value of 3.33 eV. The Pt 4f_{7/2} peak lying at around 71.0 eV can be attributed to Pt⁰ (metallic Pt), while the Pt 4f_{7/2} peak located at around 72.8 eV is related to Pt²⁺ (electrodeficient platinum) [34]. Platinum is mostly in form of Pt²⁺ on the non-stabilized tubes in agreement with the oxidation state of platinum in the precursor.

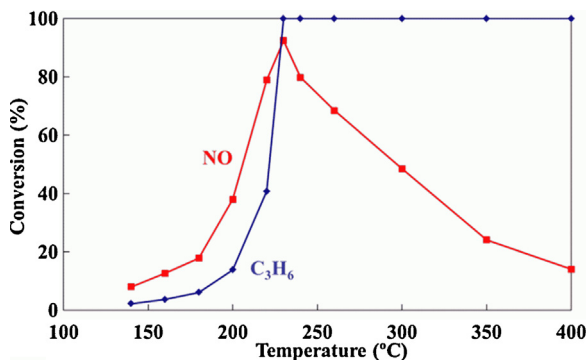


Fig. 9. NO (400 ppmv) and C₃H₆ (1500 ppmv) conversion in the presence of oxygen (3%) as a function of reaction temperature, W/F_{NO} = 2.88 g s/μmol.

The air stabilization process produces an increase and a shift of the peaks to lower binding energies, which indicate the presence of a higher contribution of platinum in form of Pt⁰ on the surface of the stabilized tubes. Probably, during the air calcination process most of the organic compounds are oxidized, producing CO among other gases, which is a reducer gas. In this sense, Cavalieri et al. [38] reported the elaboration of Pt loaded titania nanofibres and they also observed the presence of metallic Pt. They associated these results to the alcohol present as traces of solvent, or formed during the hydrolysis of the TiO₂ precursor, which reduces the Pt²⁺ in the presence of PVP, leading directly to metallic Pt nanoclusters, without the need for a subsequent reduction step [39]. However, they did not exclude that C or CO produced during the thermal decomposition of ethanol and PVP participates in reduction of Pt²⁺.

3.4. Catalytic NO conversion

The catalytic oxidation of NO and the selective catalytic reduction (SCR) of NO with propylene in the presence of oxygen with and without SO₂ and CO was studied for the platinum-loaded stabilized tubes. The concentrations of these gases in the inlet stream of the reactor were set to be similar to those found in the exhaust of combustion engines. The catalysts in mat conformation were easily introduced in a fixed bed reactor just rolling the calcined membranes, slipping the rolled mat into the reactor and packing them with compressed air. SSiT, the silica submicrotube support without platinum, showed no catalytic effect for NO conversion. However, SSiT-Pt have shown a considerably NO conversion depending on the reaction conditions, proving that platinum is readily available for catalytic activity. The addition of C₃H₆ as reducing agent to the NO-containing gas flow fed to the fixed-bed reactor resulted in NO conversion even in excess of oxygen (3%), while no NO conversion was measured when CO was used as reductant agent.

Fig. 9 shows NO and C₃H₆ conversion profiles as a function of temperature for the SSiT-Pt catalyst. A maximum NO conversion is observed at 225 °C, which lies inside the range of reported temperatures for this system, i.e., between 180 and 250 °C. Propylene also reaches full conversion at the same temperature than that for NO maximum conversion. The volcano-shape of the NO profile is characteristic of these catalytic systems. This behavior has been interpreted in terms of the competitive adsorption between NO and oxygen over the platinum active sites. At temperatures under the maximum NO conversion, the fractional coverages of NO and C₃H₆ are quite high. In this sense, the propylene combustion temperature has been delayed for 40 °C in the presence of NO (C₃H₆ conversion profile in absence of NO is not shown for clarity sake), supporting the competitive adsorption of these reactants at low temperatures. At temperatures higher than that of maximum NO conversion, O₂ adsorption is favored, being most of the active sites

occupied by oxygen. Accordingly, the adsorbed oxygen drives the propylene oxidation at such temperatures [22].

NO conversion reached a steady-state value of about 90% at 225 °C, being higher than 80% between 210 and 240 °C. The temperature window where the catalyst can operate at full condition, i.e., high NO conversion, is slightly narrower than in other platinum based catalysts reported in the literature with a similar metal loading, which also showed comparable or slightly higher conversion values at analogous reaction conditions. Nevertheless, only NO, N₂, CO₂ and H₂O were detected in the outlet gas stream up to 350 °C, indicating that the reacted NO was reduced to N₂, while all the C₃H₆ was oxidized to CO₂ and H₂O. It is important to point out that one of the main drawbacks reported in the literature for platinum catalysts is the significant selectivity toward N₂O [17–22,38,40–44]. In the tested conditions, N₂O was not detected, so its steady-state concentration, if any, would be less than 5 ppmv. Same selectivity trend was observed when propylene concentration was reduced to 400 ppm.

Fig. 10 represents the evolution of outlet gas concentration as a function of the reaction time using SSiT-Pt as catalyst for three experiments where the inlet gases were changed sequentially. For the first of them, Fig. 10a, only NO diluted in He (200 ppm, W/F_{NO} = 2.88 g s/μmol) was initially introduced in the reactor at 225 °C. After around 10 min, C₃H₆ (1500 ppm) was added to the inlet stream and, finally, at around 20 min of reaction time, O₂ (3 vol%) was also introduced. In the first step only a low adsorption of NO was observed and no reaction products were detected. With the addition of propylene to the inlet stream, NO was partially desorbed, probably due to a competitive adsorption between NO and C₃H₆ molecules taking place on the active sites. With the addition of O₂, significant reduction of NO and the complete conversion of propylene were observed.

For the second experiment, SO₂ (1000 ppm) was added and later removed from an NO/O₂ gas stream (200 ppm NO, 3% O₂) (Fig. 10b). In the first part of the experiment, partial NO oxidation to NO₂ is observed, which is linked to the well-known high activity of metallic platinum as oxidation catalyst. The addition of SO₂ to the inlet gas entirely inhibits the NO oxidation to NO₂ observed in the first step of the experiment. In this sense, Dawody et al. also reported a negative impact of SO₂ in NO oxidation by platinum in Pt/SiO₂ catalyst [45]. NO concentration in the outlet gas surpasses that of the inlet value when SO₂ was present, which could be related to unreacted NO molecules getting displaced from the adsorption sites by SO₂. This seems to be confirmed by the similar amount of NO desorbed in the second step (approx. 38 μmol/g) and the difference between removed NO and produced NO₂ in the first part of the experiment (~30 μmol/g). Furthermore, the adsorbed SO₂ amount (around 30 μmol/g) almost matches the displaced NO amount. As silica is known for showing low affinity for sulfur, the inhibition effect should be related to SO₂ adsorption over the platinum active sites. The nature of the interaction between SO₂ and platinum is reversible, as can be seen from the complete recovery of catalytic activity for NO oxidation when SO₂ was removed from the inlet gas after 120 min of reaction time.

The effect of the presence of SO₂ on NO C₃H₆-SCR conversion was also studied. Again, SO₂ (1000 ppm) was added to the inlet stream during the course of a NO C₃H₆-SCR experiment in the presence of oxygen (Fig. 10c). After 1 h, the initial gas stream composition was restored. NO conversion slightly decreased a 27.5% in the presence of SO₂ in the gas stream, while SO₂ outlet concentration soon reaches its inlet concentration. The propylene conversion slightly decreased and the selectivity toward N₂ formation remained constant. This result seems to point out that SO₂ competes preferentially with NO for adsorption over metallic platinum sites, probably due to the elevated concentration of C₃H₆ with respect to the rest of reactants. It is also interesting to observe that,

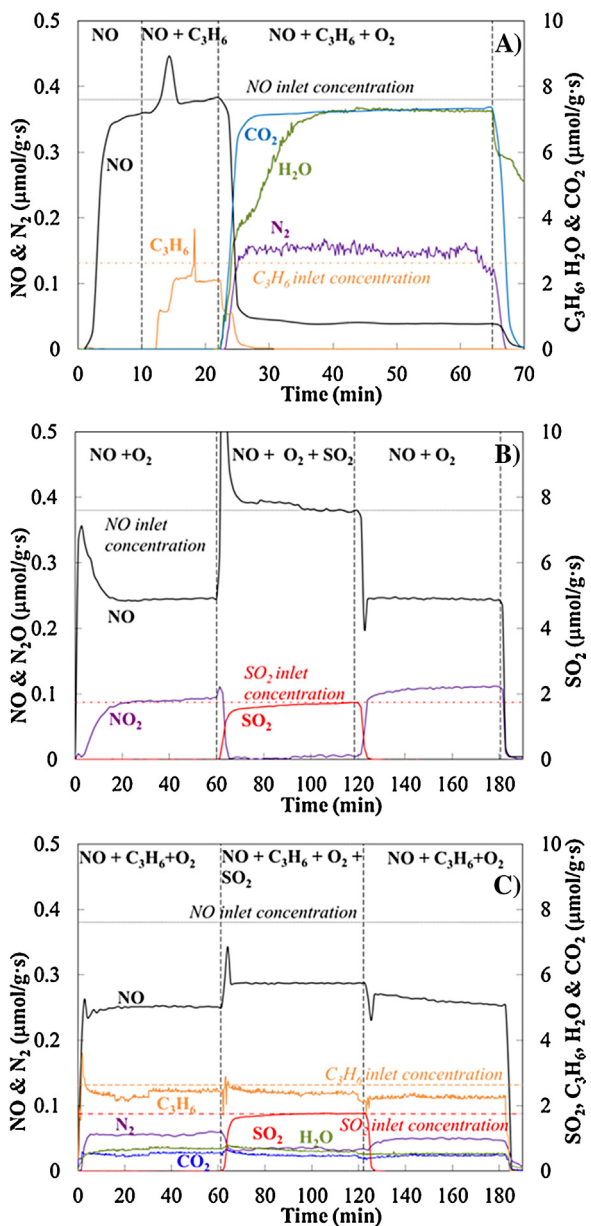


Fig. 10. Evolution of outlet gas concentration as a function of reaction time for SSiT-Pt catalyst (a) using 200 ppmv NO, 3% O₂ and 1500 ppmv C₃H₆ at 225 °C, (b) 200 ppmv NO, 3% O₂ and 1000 ppm SO₂ at 200 °C, (c) 200 ppmv NO, 1500 ppmv C₃H₆, 3% O₂ and 1000 ppm SO₂ at 200 °C.

after SO₂ has been removed from the feed stream, the catalyst activity for NO reduction is restored. Pt-loaded silica catalysts generally show high resistance to SO₂ poisoning for NO-SCR [43,45]. Neither sulfur species nor SO₂ evolution was detected by XPS or in the outlet gas during subsequent TPD after reaction, neglecting the possibility of SO₂ chemisorption or interaction with the adsorbed hydrocarbon.

The technical literature proposes two main reaction pathways for low temperature selective catalytic reduction of NO on Pt catalysts. The first one involves production of molecular nitrogen through NO dissociative adsorption via a redox mechanism [46,47]. According to this scheme, NO is adsorbed on the Pt surface and dissociates to yield adsorbed nitrogen and oxygen atoms, which desorb in the form of molecular N₂ and N₂O. The role of the reductant is to react with adsorbed oxygen atoms and regenerate the active sites. The other mechanism proposes that the activation of

the hydrocarbon play the key role in the lean-DeNO_x reaction. In this sense, the activated hydrocarbon can react with adsorbed NO or NO₂ [48–51] to form organo-nitro species that later decomposes as N₂ or N₂O. It has been also suggested that the adsorbed hydrocarbon can react with NO to form C_xH_yO_zN_w species [52,53], which would be later removed from the surface by reaction with oxygen, thus regenerating the active sites. In this sense, Djega-Mariadassou et al. reported that the mechanism is strongly influenced by the differences between the activation temperature of NO and the HC used as reductant [51].

In our case, although additional work is necessary to elucidate the most plausible reaction mechanism, it seems that the dissociative adsorption of NO cannot be disregarded, given that the main reaction pathway to produce N₂O is the reaction between an adjacent N^{*} and NO. These results suggest that no molecular NO adsorption is taken place.

On the other hand, there is some controversy regarding the role of NO₂ in NO_x SCR. In this sense, Burch et al. pointed out that the mild oxidation of HC by NO₂ is the main reaction pathway when alkanes, such as C₃H₈, are used as reductants [23]. For instance, Pitchon et al. observed NO production at low temperatures for NO₂ HC-SCR with Pt-SiO₂ catalyst, which could be pointing out that NO₂ is previously reduced to NO before N₂ formation [52]. The oxidation of NO to NO₂ in the absence of a reductant could suggest that the formation of adsorbed NO₂, which would latter interact with the adsorbed hydrocarbon, could be likely to occur on this catalytic system, although the system response in the presence of SO₂, as shown in Fig. 10b and c, seems to neglect such a possibility. Taking into account the above results, the mechanism of NO reduction through reaction between an activated hydrocarbon and NO to form C_xH_yO_zN_w species, which would later decomposed to N₂, CO₂ and water, could be also considered.

4. Conclusions

One-dimensional microstructured catalysts with well dispersed metal nanoparticles have been obtained in form of submicrometer silica tubes mats and used as catalysts in the NO reduction reaction in the presence of oxygen. The tubes have been obtained by co-axial electrospinning of a TEOS sol-gel and synthetic oil as template, using platinum (II) acetylacetone as metal precursor, followed by a calcination process. The metal nanoparticles were casted into the wall of the tube just adding the platinum precursor in the TEOS gel. Silica tubes with external/internal diameters of around 400/200 nm, respectively, and with well dispersed platinum nanoparticles of about 2 nm in size, have been obtained. The silica nanotubes doped with platinum revealed some microporosity development. These mats were tested as catalysts for the selective NO reduction reaction. The platinum loaded nanotubes show a high NO conversion when using C₃H₆ as reducing agent in the presence of oxygen, comparing fairly well with other SiO₂-Pt catalysts reported in the literature. Outstanding selectivity to N₂ at mild temperature was achieved. The presence of SO₂ during NO C₃H₆-SCR partially hinders the NO conversion, probably due to competitive adsorption between SO₂ and NO. Nevertheless, the catalytic activity of the SSiT-Pt mat was restored after removal of SO₂ from the gas inlet.

Acknowledgment

This work was supported by the Spanish Ministry of Economy and Competitiveness under CTQ2012-36408 project.

References

[1] C.M. Lieber, MRS Bull. 28 (2003) 486–491.

[2] J. Xiang, W. Lu, Y.J. Hu, Y. Wu, H. Yan, C.M. Lieber, *Nature* 441 (2006) 489–493.

[3] M. Law, J. Goldberger, P.D. Yang, *Annu. Rev. Mater. Res.* 34 (2004) 83–122.

[4] Y.N. Xia, P.D. Yang, Y.G. Sun, Y.Y. Wu, B. Mayers, B. Gates, Y.D. Yin, F. Kim, Y.Q. Yan, *Adv. Mater.* 15 (2003) 353–389.

[5] Y. Matatov-Meytal, V. Barelko, I. Yuranov, M. Sheintuch, *Appl. Catal. B: Environ.* 27 (2000) 127–135.

[6] D.H. Reneker, I. Chun, *Nanotechnology* 7 (1996) 216–223.

[7] Z.-M. Huang, Y.-Z. Zhang, M. Kotaki, S. Ramakrishna, *Compos. Sci. Technol.* 63 (2003) 2223–2253.

[8] I.G. Loscertales, A. Barrero, M. Márquez, R. Spretz, R. Velarde-Ortiz, G. Larsen, *J. Am. Chem. Soc.* 126 (2004) 5376–5377.

[9] G. Larsen, R. Velarde-Ortiz, K. Minchow, A. Barrero, I.G. Loscertales, *J. Am. Chem. Soc.* 125 (2003) 1154–1155.

[10] M. Lallave, J. Bedia, R. Ruiz-Rosas, J. Rodríguez-Mirasol, T. Cordero, J.C. Otero, M. Marquez, A. Barrero, I.G. Loscertales, *Adv. Mater.* 19 (2007) 4292–4296.

[11] R. Ruiz-Rosas, J. Bedia, M. Lallave, I.G. Loscertales, A. Barrero, J. Rodríguez-Mirasol, T. Cordero, *Carbon* 48 (2010) 696–705.

[12] I.G. Loscertales, A. Barrero, I. Guerrero, R. Cortijo, M. Márquez, A.M. Gañán-Calvo, *Science* 295 (2002) 1695–1698.

[13] J.E. Díaz, A. Barrero, M. Marquez, I.G. Loscertales, *Adv. Funct. Mater.* 16 (2006) 2110–2116.

[14] R.D. Gonzalez, T. Lopez, R. Gomez, *Catal. Today* 35 (1997) 293–317.

[15] R. Ruiz-Rosas, J. Bedia, J.M. Rosas, M. Lallave, I.G. Loscertales, J. Rodríguez-Mirasol, T. Cordero, *Catal. Today* 187 (2012) 77–87.

[16] M. Khosravi, C. Sola, A. Abedi, R.E. Hayes, W.S. Epling, M. Votsmeier, *Appl. Catal. B: Environ.* 147 (2014) 264–274.

[17] E. Santillan-Jimenez, V. Miljković-Kocić, M. Crocker, K. Wilson, *Appl. Catal. B: Environ.* 102 (2011) 1–8.

[18] E. Santillan-Jimenez, Mark Crocker, A. Bueno-López, C. Salinas-Martínez de Lecea, *Ind. Eng. Chem. Res.* 50 (2011) 7191–7200.

[19] R. Burch, P.J. Millington, *Catal. Today* 26 (1995) 185–206.

[20] J.M. García-Cortés, J. Pérez-Ramírez, J.N. Rouzeaud, A.R. Vaccaro, M.J. Illán-Gómez, C. Salinas-Martínez de Lecea, *J. Catal.* 218 (2003) 111–122.

[21] J.M. García-Cortés, J. Pérez-Ramírez, M.J. Illán-Gómez, F. Kapteijn, J.A. Moulijn, C. Salinas-Martínez de Lecea, *Appl. Catal. B: Environ.* 30 (2001) 399–408.

[22] R. Burch, P.J. Millington, *Catal. Today* 29 (1996) 37–42.

[23] R. Burch, T.C. Watling, *Appl. Catal. B: Environ.* 17 (1998) 131–139.

[24] S.J. Gregg, K.S.W. Sing, *Adsorption, Surface Area and Porosity*, 2nd ed., Academic Press, London, 1982.

[25] M.A. Vannice, *Kinetics of Catalytic Reactions*, Springer, New York, USA, 2005, pp. 20.

[26] R.J. Farrauto, C.H. Bartholomew, *Fundamentals of Industrial Catalytic Processes*, Blackie Academic & Professional, NY, 1997.

[27] J.C.O. Santos, I.M.G. Santos, M.M. Conceição, S.L. Porto, M.F.S. Trindade, A.G. Souza, S. Prasad, V.J. Fernandes, A.S. Araújo, *J. Therm. Anal. Calorim.* 75 (2004) 419–428.

[28] W.L. Huang, S.H. Cui, K.M. Liang, Z.F. Yuan, S.R. Gu, *J. Phys. Chem. Solids* 63 (2002) 645–650.

[29] R.S. McDonald, *J. Am. Chem. Soc.* 62 (1958) 1168–1178.

[30] A.C. Patel, S. Li, C. Wang, W. Zhang, Y. Wei, *Chem. Mater.* 19 (2007) 1231–1238.

[31] F. Rodríguez-Reinoso, J. Garrido, J.M. Martín-Martínez, M. Molina-Sabio, R. Torregrosa, *Carbon* 27 (1989) 23–32.

[32] Z. Lin, M.D. Woodrooff, L. Ji, Y. Liang, W. Krause, X. Zhang, *J. Appl. Polym. Sci.* 116 (2010) 895–901.

[33] A. Katz, M.E. Davis, *Nature* 403 (2000) 286–289.

[34] J.F. Moulder, W.F. Stickle, P.E. Sobol, K.D. Bomben, in: J. Chastain, R.C. King Jr. (Eds.), *Handbook of X-ray Photoelectron Spectroscopy*, Physical Electronics, Inc., Eden Prairie, MN, 1995.

[35] R.J.P. Corriu, D. Leclercq, P.H. Mutin, A. Vioux, *Mater. Res. Soc. Symp. Proc.* 346 (1994) 351–356.

[36] G.D. Sorarù, G. D'Andrea, A. Glisenti, *Mater. Lett.* 27 (1996) 1–5.

[37] G.M. Ingo, C. Riccucci, G. Bultrini, S. Dirè, G. Chiozzini, *J. Therm. Anal. Calorim.* 66 (2001) 37–46.

[38] S. Cavalieri, S. Subianto, L. Chevallier, D.J. Jones, J. Rozière, *Chem. Commun.* 47 (2011) 6834–6836.

[39] N. Toshima, *Macromol. Symp.* 105 (1996) 111–118.

[40] J.M. García-Cortés, M.J. Illán Gómez, C. Salinas Martínez de Lecea, *Appl. Catal. B: Environ.* 74 (2007) 313–323.

[41] S.-C. Shen, S. Kawi, *J. Catal.* 213 (2003) 241–250.

[42] P. Denton, A. Giroir-Fendler, H. Praliaud, M. Primet, *J. Catal.* 189 (2000) 410–420.

[43] S.-C. Shen, S. Kawi, *Appl. Catal. B: Environ.* 45 (2003) 63–76.

[44] A. Bueno-López, M.J. Illán-Gómez, C. Salinas-Martínez de Lecea, *Appl. Catal. A: Gen.* 302 (2006) 244–249.

[45] J. Dawody, M. Skoglundh, L. Olsson, E. Fridell, *J. Catal.* 234 (2005) 206–218.

[46] R. Burch, P.J. Millington, A.P. Walker, *Appl. Catal. B: Environ.* 4 (1994) 65–94.

[47] R. Burch, J.A. Sullivan, *J. Catal.* 182 (1999) 489–496.

[48] G.P. Ansell, A.F. Diwell, S.E. Golunski, J.W. Hayes, R.R. Rajaram, T.J. Truex, A.P. Walker, *Appl. Catal. B: Environ.* 2 (1993) 81–100.

[49] D.K. Captain, C. Mihut, J.A. Dumesic, M. Amiridis, *Catal. Lett.* 83 (2002) 109–114.

[50] V. Pitchon, A. Fritz, *J. Catal.* 186 (1999) 64–74.

[51] G. Djega-Mariadassou, F. Baudin, A. Khacef, P. Da Costa, in: V.I. Parvulescu, M. Magureanu, P. Lukes (Eds.), *Plasma Chemistry and Catalysis in Gases and Liquids*, Wiley-VCH, 2012, pp. 89–129.

[52] F. Garin, P. Girard, S. Ringler, G. Maire, N. Davias, *Appl. Catal. B: Environ.* 20 (1999) 205–218.

[53] O. Gorce, F. Baudin, C. Thomas, P. Da Costa, G. Djéga-Mariadassou, *Appl. Catal. B: Environ.* 54 (2004) 69–84.